Comparison of Lyman-Alpha and LICOR infrared hygrometers for measuring airborne turbulent fluctuations of water vapor

Astrid Lampert[1], Jörg Hartmann[2], Falk Pätzold[1], Lennart Lobitz[1], Peter Hecker[1], Katrin Kohnert[3], Eric Larmanou[3,4], Andrei Serafimovich[3], and Torsten Sachs[1,3]

[1]Institute of Flight Guidance, TU Braunschweig, Hermann-Blenk-Str. 27, 38108 Braunschweig, Germany
[2]Alfred Wegener Institute for Polar and Marine Research, Bussestr. 24, 27570 Bremerhaven, Germany
[3]GFZ German Research Centre for Geosciences, Telegrafenberg, 14473 Potsdam, Germany
[4]Swedish University of Agricultural Sciences, Umeå, Sweden

Correspondence to: Astrid Lampert (Astrid.Lampert@tu-braunschweig.de)

Abstract. To investigate if the LICOR humidity sensor can be used as a replacement of the Lyman-Alpha sensor for airborne applications, the measurement data of the Lyman-Alpha and several LICOR sensors are analysed in direct intercomparison flights on different airborne platforms. One vibration isolated closed-path and two non-isolated open path LICOR sensors were installed on a Dornier 128 twin engine turbo-prop aircraft. The closed-path sensor provided absolute values and fluctuations of the water vapour mixing ratio in good agreement with the Lyman-Alpha. The signals of the two open-path sensors showed considerable high frequency noise, and the absolute value of the mixing ratio was observed to drift with time in this vibrational environment.

On the helicopter-towed sensor system Helipod with very low vibration level the open-path LICOR sensor agreed very well with the Lyman-Alpha over the entire frequency range up to 3 Hz.

The results show that the LICOR sensors are well suited for airborne measurements of humidity fluctuations, provided that a vibrationsless environment is given, and this turns out to be more important than close sensor spacing.

1 Introduction

Water vapour and clouds in the atmosphere have a large impact on the energy balance (Ramanathan et al., 1989), the hydrologic cycle (e.g. Chahine, 1992) and on local and global climate (Trenberth et al., 2007; Zhou et al., 2011). Therefore, accurate knowledge of atmospheric water vapour concentration and transport is of high relevance for understanding climate and climate change. A general increase in atmospheric moisture measured at the surface and humidity within the troposphere has been reported (IPCC, 2013). Satellite retrievals of the vertical water vapour distribution provide limited spatial resolution, e.g. 300 m in the vertical and 30 km in horizontal direction (Bender et al., 2011). The most effective way for moisture transport from the surface to the atmosphere is turbulence. Turbulent fluxes are commonly determined with the eddy-covariance method. This technique requires accurate and high resolution measurements of the fluctuations of the vertical component of wind speed and humidity.

For the quantification of atmospheric processes on local to regional scales, airborne measurements are required to fill the

gap between large-scale, low resolution information from satellites and measurements at fixed locations, as towers, providing higher vertical and temporal resolution.

For *in situ* measurements of humidity, the error bars are typically larger than for other atmospheric parameters like temperature and wind. In the troposphere, the water vapour concentration in ppm varies over two orders of magnitude (e.g. Schneider et al., 2010). Since measuring atmospheric water vapour precisely is difficult, the uncertainties of atmospheric water vapour measurements are high. Even with the best systems under well controlled conditions in the laboratory, there are large discrepancies between different measurement systems, e.g. intercomparison measurements of different hygrometers probing the same air simultaneously revealed discrepancies between different measurement systems of around 10 % (Fahey et al., 2014). For cold and dry conditions, as encountered in the upper troposphere and lower stratosphere, the instruments had a variation around the reference value of 20 % (Fahey et al., 2014).

Airborne sensors have to fullfil specific requirements. On the one hand, a high temporal resolution is needed in order to obtain a high spatial resolution for the moving platforms. On the other hand, long-term stability and high accuracy, if possible without the need of frequent re-calibration, are essential. In practice, as no sensor is available that meets both requirements, this leads to the combination of complementary sensors for both high resolution and long-term accuracy.

In the following, the measurement principles of the different humidity sensors used in this study are shortly summarized.

1.1 Material absorption

Capacitive sensors are based on taking up humidity in a porous or hygroscopic material, changing the dielectric properties. An example is the Vaisala Humicap sensor, which is used as the standard for radiosondes. However, the response times for increasing and decreasing humidity may differ significantly due to the different diffusion coefficient into the material and out of the material, and the temporal resolution is limited. For temperatures exceeding $0\,°C$, and with the help of extensive postprocessing or modelling, the relatively slow polymer-based absorption hygrometers are sometimes used for retrieving humidity fluctuations (Wildmann et al., 2014).

The typical calibration procedure consists of applying saturated salt solutions with different known relative humidities, and recording the sensor output, thus creating a calibration curve. The sensor is sensitive to contamination by e.g. sea salt, which may alter the sensor properties significantly, making a regular cleaning and re-calibration necessary.

1.2 Atomic absorption

Sensors based on atomic absorption provide the advantage of a very fast response time allowing for measurement frequencies exceeding 100 Hz, a sharp absorption line compared to the absorption bands of molecules, and a high degree of absorption. This requires measurement cells of only few millimeters (Buck, 1973). The sensor is based on the emission of ultraviolet (UV) radiation at a wavelength of 121.56 nm (transition of an electron from the first excited state n=2 to the ground state n=1 in the hydrogen atom, called Lyman-Alpha emission line). As the Lyman-Alpha wavelength is strongly absorbed by water vapour,

the signal in the ion chamber detector is weakened accordingly. The relation is given by the attenuation law of Lambert-Beer. The absorption of the Lyman-Alpha line has cross sensitivities with oxygen and ozone molecules. The absorption by oxygen molecules is about 1000 times weaker than by ozone molecules, and can be corrected by taking into account pressure and temperature, as the fractional density is constant. The correction of the absorption by ozone molecules (same order of magnitude

5 with respect to water vapour) is only necessary in the stratosphere (Buck, 1976).

Calibration is done by applying air of known humidities and recording the detector signal as a calibration curve. The aging of the lamp, or degradation of the magnesium fluoride windows, lead to a reduced signal strength with time, which is interpreted as higher absorption, thus higher water content. This (slow) drift makes a regular calibration of either the sensor or the retrieved data necessary.

10 The term "Lyman-Alpha" in this paper is used as a synonym for the Lyman-Alpha absorption hygrometer by Buck Research (Buck, 1973, 1976). It has been operated as the standard fast humidity sensor in many research aircraft for several decades (Busen and Buck, 1995; Corsmeier et al., 2001; Drüe and Heinemann, 2007; Twohy et al., 1997). However, with the end of the life time of the radiation sources (glow discharge lamps) and difficulties in replacing them, other humidity sensors become more important, and a variety of fast-response sensors is now available, e.g. the following two sensors: A system similar to the

15 Lyman-Alpha is the Krypton hygrometer KH20 of Campbell Scientific, USA, which has a cross sensitivity to oxygen as well and therefore, like the Lyman-Alpha, has to be calibrated carefully (Foken and Falke, 2012). It is, however, mostly used for ground-based measurements. Furthermore, the instrument is very sensitive to path length, and calibration is difficult even for the ground-based applications (Foken and Falke, 2010). For the research aircraft of NCAR, a new Lyman-Alpha sensor was built, which showed promising first results (Beaton and Spowart, 2012).

1.3 Molecular absorption

Hygrometers based on molecular absorption can be sub-divided into systems based on a laser light source and the simpler and cheaper technique of using a broadband light source combined with interference filters. However, laser sources and fibre optics are now readily available as well due to advances and application in telecommunications. The disadvantage of molec-

25 ular absorption is line broadening with pressure, resulting from the impact of other molecules. These measurement systems include the Picarro greenhouse gas analyser (Crosson, 2008) and the Los Gatos Fast Greenhouse Gas analyser (Baer et al. , 2002), which measure the three most important greenhouse gases water vapour, carbon dioxide and methane simultaneously. For retrieving methane and carbon dioxide with these instruments, the water vapour measurements are necessary to reference the number concentration of methane molecules to the dry mole fraction.

30 The fast-response LICOR instruments LI-7500, LI-7500A and LI-7200 for measuring humidity are based on the absorption of near infrared radiation. They have a longer measurement path of 12.5 cm compared to the few mm of the Lyman-Alpha. The LICOR sensors in different forms are used at automated field stations for research networks covering large temporal and spatial scales, and they are therefore well characterised concerning the transfer function of different components (Metzger et al., 2016). The closed-path sensors requiring a gas sampling system can be affected by high-frequency attenuation, so inlets

and tubes have to be dimensioned reasonably (Aubinet et al., 2016; Metzger et al., 2016).

Like for the Lyman-Alpha, the attenuation of the signal obeys the law of Lambert-Beer relating absorptance to the number density of the absorbing gas, taking into account pressure, and requires correction terms due to cross-sensitivities. The calibration procedure consists of applying air of well-defined humidity for two points, and adapting the calibration coefficients
5 accordingly. Zero signal is created by dry, carbon dioxide free gas. The second point can be applied e.g. with the LICOR dew point generator.

The LICOR humidity sensors have been used for airborne applications additionally to the Lyman-Alpha or to replace the Lyman-Alpha for many years (Beringer et al., 2011; Pillai et al., 2011; Hiller et al., 2014). The sensors have been implemented in various configurations, some facing with the sensor head forward, e.g. on the helicopter borne sensor system Helipod, and
10 the Airborne Cloud Turbulence Observation System ACTOS (Siebert et al., 2013), some with the sensor head oriented vertical (French Piper Aztec research aircraft), some with an open housing (Siebert et al., 2013), some with a metal grid (Helipod), some with additional purging with synthetic air to keep the detector free of water vapour (Schmitgen et al., 2004).

The manufacturer warns in the manual that the sensor should not be applied at vibrations around 150 Hz and around the harmonics (Licor, 2014). However, the impact on measurements is not specified or even quantified. As the LICOR sensor
15 is currently the cheapest fast-response water vapour sensor commercially available, and small enough to be easily integrated into aircraft, its airborne applications will very likely increase. Therefore, knowing the limitations of the LICOR sensors with respect to vibrations is important, and one of the main aims of this study.

For large research aircraft, some specifically designed hygrometers are implemented: On the National Science Foundation Gulfstream-V aircraft, a cavity diode laser hygrometer with two absorption lines in the near-infrared is deployed with a tem-
20 poral resolution of 25 Hz (Zondlo et al., 2010). On the NASA ER-2 aircraft, a specifically designed near-infrared tunable diode laser spectrometer is deployed for measuring atmospheric water vapour concentration (May, 1998), with a sampling rate of 1 Hz and 10% accuracy (Herman et al., 2017). On the DLR HALO (High Altitude Long-Range Aircraft), another spectroscopic sensor developed by the Physikalisch-Technische Bundesanstalt (PTB) Braunschweig is deployed (Buchholz et al., 2014). Compared to the LICOR sensor, this tunable diode laser hygrometer can be operated much faster (up to several kHz)
25 and with a known accuracy, providing the most precise humidity values available to date (Buchholz et al., 2013, 2014, 2016). However, this hygrometer requires extensive post processing, and at least so far it is not possible to obtain real-time humidity data. The spectroscopic sensors are experimental systems and not commercially available.

The aims of this article are (1) to show limitations and provide information for successful handling for the airborne use of LICOR humidity sensors, (2) to quantitatively compare fluxes of latent heat obtained with the former "standard" Lyman-Alpha
30 and with the LICOR sensors for airborne applications, and (3) to determine the required measurement frequency for humidity fluctuations to derive reliable latent heat fluxes for the typical flight altitude of a few 100 m and airspeed in the range of 35 to 70 m s^{-1}.

2 Experimental setup

This section provides the background of the sensors used in the study, including a short overview of the LICOR sensor working principle, and a description of the airborne platforms and their sensor setup. For the flights, both a Lyman-Alpha and at least one LICOR sensor were operated in parallel, and the latent heat fluxes derived from the different humidity sensors and the same wind vector measurements are compared directly.

2.1 LICOR sensors

The working principle of the LICOR sensor series for water vapour and carbon dioxide (CO_2) is the absorption of near infrared radiation by these molecules. The radiation source is a small lamp with broadband emissions in the near infrared (NIR) spectral range. The radiation is focussed on a filter wheel with bandpass filters of different wavelengths, rotating at a speed of 150 Hz. The light at a wavelength of 2590 nm is absorbed by water vapour but not by carbon dioxide, the light at a wavelength of 4260 nm by CO_2, but not by water vapour, and the light at a wavelength of 3950 nm serves as a reference, where neither CO_2 nor water vapour have absorption bands. The narrow band-pass filtered radiation then passes the measurement cell of 12.5 cm length, where the ambient air either passes passively (open path sensor, LI-7500, and the newer LI-7500A) or is pumped through (closed path sensor, LI7200), and partly absorbs radiation depending on the number density of the absorbing water molecules, as well as for the CO_2 concentration. The detector on the other side of the measurement cell is a thermopile, additionally cooled by Peltier elements. The system is described in more detail in Licor (2014). The data sampled internally at 150 Hz frequency is processed and provided at a maximum frequency of 20 Hz. The time offset for internal processing is specified for the LI-7500 as 0.185 s, and for both the LI-7500A and LI-7200 as 0.130 s.

2.2 Do128 instrumentation

The standard meteorological equipment of the research aircraft Do128 "D-IBUF" of the Institute of Flight Guidance, TU Braunschweig, consists of a five-hole probe and corresponding Setra pressure transducers (static, dynamic and differential pressure), inertial navigation and global navigation satellite system (GNSS) for deriving the 3D wind vector (see description of methods by e.g. van den Kroonenberg et al., 2008; Bärfuss et al., 2018), a long-time stable Rosemount DB102 temperature sensor with slow response time of around 1 s, and a fast response (100 Hz) Rosemount EL102 temperature sensor. The temperature sensors are mounted in a sophisticated Rosemount inlet to directly obtain the static air temperature, and can additionally be heated for flights in icing conditions. The humidity channel includes a dew point mirror TP 3-S of Meteolabor (not operational for this study), a capacitive humidity sensor (Vaisala HMP233 Humicap) and a Lyman-Alpha optical sensor L-6 / HMS-2 of Buck Research. Further, a surface temperature sensor KT15 is included. Temperature and humidity sensors, as well as the five-hole probe are integrated into the nose boom. More details on the instrumentation can be found in Hankers (1989); Bange et al. (2002); Corsmeier et al. (2001, 2002). The Vaisala Humicap is calibrated before and after each measurement campaign by

applying saturated salt solutions and their different known equilibrium relativ humidity, and the combined signal of the slow Humicap and the fast Lyman-Alpha has been shown to agree well with other independent measurements of humidity (Sodemann et al., 2017).

For the humidity intercomparison flight, three different LICOR systems were available (open path LI-7500 with serial number 75H-0775, open path LI-7500A with serial number 75H-2287, and closed-path LI-7200 with serial number 72H-0584). The two open path sensors were covered by a metal grid to enforce turbulent mixing and avoid gradients of concentration in the measurement cell. The three LICOR sensors were installed in addition to the standard equipment at the following locations: on the nose boom (LI-7500A, in the following called Li1), in the cabin directly under the roof (LI-7200, called Li2), with an inlet sampling the air near the LI-7500 (called Li3) on the roof (see Fig. 1). The axis of the optical path of all sensors were oriented along the aircraft longitudinal axis. No purging of the sensors with nitrogen or dried air was applied.

The stainless steel inlet to the Li2 sensor had a length l_1 of 350 mm, an inner diameter of 9.6 mm, resulting in an area of $A_1 = 7.24 \cdot 10^{-5} m^2$. A volume flow controller provided a flow of $Q = 15 \, l \, min^{-1} = 2.5 \cdot 10^{-4} \, m^3 \, s^{-1}$. For the tube, the airspeed is therefore $v_1 = \frac{Q}{A_1} = 3.45 \, m \, s^{-1}$. This results in a time shift $\Delta t_1 = \frac{l_1}{v_1} = 0.1 \, s$. Similar calculations are applied for the nylon tube of length $l_2 = 400$ mm and inner diameter of 8 mm, guiding the air from the inlet to the sensor, which results in an additional time shift of 0.03 s. Additionally, the time for exchanging the air of the measurement cell with an inner diameter of 25 mm and a half length of 125 mm amounts to 0.12 s. Altogether, there is a time shift of 0.25 s caused by the sampling system for the Li2. For the humidity intercomparison flight, vibration sensors of type M3555B04/03/02 and M356B18 of the company PCB Piezotronics Inc., US, were integrated along the x-axis (perpendicular to flight direction) and z-axis (upward directed) of the LICOR sensors. For the Li2, another vibration sensor in y direction (in flight direction along the aircraft and the sensors) was available.

2.3 Synchronisation of the Do128 humidity sensors

Before calculating the humidity fluctuations, the four fast humidity sensors (Lyman-Alpha, Li1, Li2, Li3) onboard the Do128 located at different places were synchronised. As mentioned in Sect. 2.2, the Lyman-Alpha and the Li1 are located at the nose boom, the Li3 at the cabin roof, and the inlet of the Li2 is close to the Li3 on the cabin roof. First the Lyman-Alpha data were shifted in time against the vertical wind speed by maximizing the turbulent latent heat flux. The synchronisation was then done by maximizing the covariance of the mixing ratio fluctuations of the Lyman-Alpha and each of the LICOR sensors for varying temporal offsets. The time step providing the highest correlation was used as the time shift between the sensors. The time signal of the Lyman-Alpha was used as reference. The part of the flight used for the synchronisation (shaded in grey in Fig.3) contains large variability in the signals (changes of altitude, and high fluctuations), facilitating to derive a high correlation of the signals. The time shift between the Lyman-Alpha and the Li1 sensor in the nose boom was 0.15 s. As stated in the LI7500A manual, an internal time shift of 0.13 s is caused by data processing. The remaining small difference of 0.02 s may be explained by the sampling geometry, as the Li1 is covered by a sheet metal as explained in Sect. 2. The time shift between the Lyman-Alpha and the Li3 sensor at the cabin roof was 0.3 s. Therefore, the time shift between the two open path sensors Li1 and Li3 amounted to

0.15 s. This can be well explained by the different internal time shift of 0.13 s for the Li1 and 0.185 s for the Li3, amounting to 0.05 s, plus additionally the distance δs of 7 m between the two sensors (Li1 installed at the nose boom, Li3 at the cabin roof) and the true airspeed v_{tas} of $70 \, \mathrm{m \, s^{-1}}$:

$$\Delta t = \frac{\Delta s}{v_{tas}} = \frac{7 \, m}{70 \, m \, s^{-1}} = 0.1 \, s \tag{1}$$

5   The time shift between the Lyman-Alpha and the Li2 in the cabin was 0.45 s. Subtracting the values for the time shift caused by the distance (0.1 s) and the internal time shift (0.13 s), this results in a time difference of 0.22 s. This time shift can be explained by the tube length and flow speed for guiding the air to the measurement cell in the cabin, as calculated in Sect. 2.

For further calculations, the best fitting time shift correction was applied to all three LICOR sensors. The correlation between the LICOR signals and the Lyman-Alpha was better than 0.95 for the Li2 and Lyman-Alpha, and exceeding 0.8 for the Li1 and

10   Lyman-Alpha for the part of the flight considered here. The best correlation between Li3 and Lyman-Alpha amounted to 0.6, thus was considerably lower (Fig.9).

The calculations of the best fitting time shift were verified by maximizing the coherence spectra of the LICOR sensors and the Lyman-Alpha as a reference, and at the same time minimizing the phase between the two signals. This resulted in the same time shift as determined by the method of maximizing the correlation.

15   **2.4   Helipod instrumentation**

The data of a measurement flight with the "Helipod", a meteorological sensor system towed by rope to a helicopter (e.g., Bange and Roth, 1999; Bange et al., 2002; Martin and Bange, 2014), is analysed here. The Helipod is equipped with different meteorological sensors: Humidity measurements are performed with a Lyman-Alpha sensor L6 of Buck Research, US, a capacitive Vaisala Humicap HMP110, a dew point mirror 1011B of General Eastern, US (not used for this study), and the LI-7500 (same

20   sensor as used for the Do128 flight, there called Li3). Temperature is measured with a Pt100 by Rosemount, and a fine wire by Dantec. A five-hole probe with the same differential pressure sensors as in the Do128 is integrated (D289 for differential pressure, D270 for static pressure, Setra, US), as well as a GPS system with eight receivers for a full 3D attitude alignment (GNATTI System of Geo++ GmbH, Germany) and IMU (LCR 88, LITEF, Germany). A Heimann KT19 sensor (Heimann, Germany) records the surface temperature. Altitude information is provided by GPS, barometric pressure, and a radar altimeter

25   ERT180 (Thomson-CFS, France).

2.5   Synchronisation of the Helipod humidity sensors

As the LI-7500 system was calibrated directly before the measurement campaign, and therefore provides reliable absolute values, the Lyman-Alpha values of the mixing ratio were calibrated against the LICOR data using a linear regression method.

30   Before calculating turbulent fluxes of latent heat, the time shift between the LICOR and the Lyman-Alpha was corrected by calculating the maximum coherence with minimum phase shift of the two signals. The best correlation was found for a total time shift of 0.315 s. This includes the time shift caused by internal processing of 0.186 s, plus an additional time shift of around

0.13 s. The additional time lag may be attributed to the semi-open housing geometry. This value was confirmed by calculating the best correlation between the time series. The time lag was the same for straight and level flight sections throughout three campaigns in Siberia in April, June and August 2014.

3 Flights and atmospheric conditions

3.1 Do128 flight on 23 October 2015

The measurement flight with the research aircraft Do128 "D-IBUF" was conducted on 23 October 2015. The aircraft operates at a true airspeed of $70\,\mathrm{m\,s^{-1}}$. The flight was performed above different terrain of the North German Plain, including areas dominated by forest, by agricultural farmland, and above open water North of the East Frisian Islands (Fig. 2). The part of the flight that was used for the sensor comparison is displayed in white on the flight track (Fig. 2) and grey shaded in Fig. 3, which fullfills the requirements of Lenschow et al. (1994) for the sampling length for several sub-legs above homogeneous terrain. Such small sub-legs were chosen with different but homogeneous surface conditions and different but constant flight altitudes to compare if there are systematic differences in the parameters like the vibration level.

The flight took place under varying cloud conditions, mostly overcast with a cloud bottom at an altitude of around 1000 m. Above land, a neutrally stratified boundary layer was observed up to an altitude of around 1000 m, with a strong increase of potential temperature of 6 K in 1000 to 1200 m. However, above the North Sea, the atmosphere was stably stratified. Therefore, significant latent heat fluxes were only observed over land.

3.2 Helipod flight on 14 August 2014

The overall aim of the Helipod measurements was to study greenhouse gas emissions on a climatically relevant sub-regional scale of up to 100 km to investigate the spatial variability, and to analyse how representative the continuous emission measurements on local scales are on this larger scale. During the measurement flight, the Helipod was attached to a Russian Mi8 helicopter by a 30 m rope. The flight was performed at a true airspeed of $40\,\mathrm{m\,s^{-1}}$ from the Research Station Samoylov Island in the Lena Delta, Siberia.

The Helipod flight analysed here took place on 14 August 2014, when seasonal thawing of the active layer on top of the permafrost was still in progress. The roundtrip flight pattern followed a 100 km horizontal leg at 100 m altitude in north-western direction with vertical profiles up to 1500 m altitude at both ends of the leg. The atmosphere was neutrally stratified in the lowermost 150 m, then slighly stable up to 1000 m (increase in potential temperature smaller than 1 K from the surface up to that altitude), and the ABL top was evident by an increase of potential temperature at 1000 m altitude.

The flight on 14 August 2014 was done in conditions nearly free of clouds at the beginning with a near-surface air temperature around $17\,^{\circ}\mathrm{C}$ and southerly wind with a speed of $5\,\mathrm{m\,s^{-1}}$ near ground. The mean wind speed at the altitude of the Helipod transects was $8\,\mathrm{m\,s^{-1}}$, and the mean wind direction at that altitude was $180\,^{\circ}$. For this instrumental intercomparison, the first

long flight transect from Samoylov Station to Arga-Muora is analysed (Fig. 4). On the way back, short rain showers were encountered. The time series of the height, vertical wind speed, mixing ratio, potential temperature and valid data is shown in Fig.5.

4 Results

4.1 Vibrations during the Do128 flight

The time series of the mixing ratio (Fig. 3) shows the general behaviour of the Li2 sensor, the slow Humicap and the fast Lyman-Alpha sensor. The time periods affected by radio communication were excluded from further analyses, as they occasionally induce artificial spikes on the Lyman-Alpha sensor. The data used for calculating the spectra are shaded in grey. They were chosen to exclude the flights at higher altitude, where the signal of the Lyman-Alpha differs significantly from the other sensors. Under these different pressure conditions, a different sensitivity range would be necessary, which was not adapted during the flight. For the data of the Li1 and Li3, different effects can be observed:

- The signals of the open path sensors Li1 and Li3 contain a higher level of noise compared to the closed path Li2 system and the signal of the Lyman-Alpha.

- Changes in altitude affect the signals of Li1 and Li3, and the absolute values of the mixing ratio do not follow the behaviour of the Li2 and the Humicap. This might be caused by changing vibration environments due to different power settings.

- There is a general slow drift in the signal of the open path sensors Li1 and Li3, which does not follow the trend of the closed path Li2 sensor, the signal of Lyman-Alpha, and Humicap.

Differences are apparent in the time series of the vibrations (Fig. 6): The amplitude of acceleration in z direction is around $50\,\mathrm{m\,s^{-2}}$ for the Li3, around $40\,\mathrm{m\,s^{-2}}$ for the Li1 and around $3\,\mathrm{m\,s^{-2}}$ for the Li2 sensor. The example shows a small flight section of 3 min, indicated in yellow in Fig. 3, but is representative for sections of this length at constant altitude.

The acceleration spectra for all three sensors in y and z direction (along sensor and aircraft axis, and vertical direction) as well as x direction (perpendicular to sensor and flight direction) for the Li2 sensor are shown in Fig. 7 for a short flight section of 3 min. Strong and sharp vibration peaks at distinguished frequencies were recorded at the locations of all sensors, as well as differences in the broadband features.

Generally, the acceleration for high frequencies (exceeding 200 Hz) is several orders of magnitude lower for the Li2 sensor compared to the Li1 and Li3 sensors. This feature gets more pronounced for frequencies exceeding 1000 Hz. The strength of vibrations contained within individual peaks is more pronounced for the Li1 and Li3 sensor compared to the Li2 sensor. In Fig.7, the critical frequencies of 150 Hz and higher harmonics, as specified by the manufacturer, are indicated by vertical black lines. Especially around 450 Hz it can be seen that the vibration level of the Li3 is more than an order of magnitude higher than the vibration level of the Li1. This feature is observed during all flight legs analysed here, persistent throughout each flight

leg. The high level of vibrations at the critical frequencies and potential impact on the internal signal processing could be an explanation for the different humidity spectra shown in the following.

4.2 Powerspectra of humidity fluctuations

5   The above mentioned properties of the sensors are reflected in the spectra of the mixing ratio, shown in Fig. 8 for each humidity signal. The sloped lines represent the -5/3 drop-off expected in the inertial subrange. Between 0.003 and 0.3 Hz all sensors follow the Kolmogorov prediction (Kolmogorov, 1941) very well, and those of the Lyman-Alpha and Li2 continue for a further decade, while Li1 and Li3 level off indicating a substantial level of white noise superimposed on the humidity signal. The Humicap spectrum gradually decreases slightly faster.

10   Overall, the Lyman-Alpha spectrum most closely behaves as expected from the theory, and the Li2 spectrum is very similar but drops off marginally faster beyond 1 Hz. This behaviour can be attributed to somewhat increased dampening due to longer inlet tubes in comparison to those for the Lyman-Alpha.

At low frequencies the Vaisala Humicap and even more the Li3 sensor show higher variances. It will be shown in the next subsection that this variance is differently correlated with the vertical wind velocity, which has implications for the flux calcu-

15   lation.

4.3 Cospectral analysis

As the Lyman-Alpha humidity sensor has been used widely in turbulence studies over decades, it is taken as a reference to compare the behaviour of the other sensors. Cospectra between each of these other sensors and the Lyman-Alpha are calculated. Based on the grey shaded data set of Fig.3, Fig.9 shows the coherence and the phase of the different LICOR sensors with the

20   Lyman-Alpha. Li2 provides the best coherence with Lyman-Alpha, virtually equal to one over a large frequency range of three decades. It only drops off for frequencies beyond 1 Hz due to the spatial separation of the two sensors. No phase difference is observed over the same frequency range. In the phase spectrum the coherence is coded in the thickness of the dots as a phase can only be interpreted if a significant coherence between the signals is present. The marginally positive phase between Li2 and Lyman-Alpha is a result of the advancement of the Li2 signal over 0.315 s. This constant shift can only approximate the

25   more complex difference in the high-frequency response behaviour between Li2 and Lyman-Alpha due to spacing and tubing. A smaller advancement, however, leads to reduced coherence and a trailing phase shift of Li2 for frequencies below 1 Hz. The other two LICOR sensors (Li1 and Li3) have far less coherence with the Lyman-Alpha. At low frequencies this reflects the drift of both vibration affected sensors, and at high frequencies the noise fades more coherence that might exist. Note that for all three LICOR sensors the coherence inversely correlates with the amount of vibration the sensors are exposed to. The

30   response behaviour of the Vaisala Humicap is more complex. At low frequencies (<0.01 Hz) it agrees reasonably well with the Lyman-Alpha. Then the coherence decreases with increasing frequency. The phase shift disappears around 0.4 Hz, but the level of coherence remains lower. To assess the sensor behaviour on the moisture flux calculation, Figure 9 (right) shows the covariance of the vertical wind speed and the humidity values from the different sensors after correction of the time shift.

The spectral estimates are multiplied by the frequency, thus the area below the curves is proportional to the humidity flux. Flux estimates based on Li2 and Lyman-Alpha reasonably agree, but those calculated by the vibration affected LICOR sensors are too low, most pronounced for Li3. The Humicap shows an interesting behaviour: overestimation on a scale of minutes (0.02 Hz) and underestimation for higher frequencies, both of which compensate to a certain degree. This behaviour seems to be a specific property of the Vaisala Humicap sensor. The latent heat flux determined with the Humicap amounts to 95% of the reference value determined with the Lyman-Alpha. Thus, for moderate conditions (10-20°C, humidity values typical for midlatitudes), the Humicap can be used for determining airborne latent heat fluxes with an acceptable error bar. However, the response function of the Humicap is asymmetric, with a different response time for decreasing and increasing humidity, and the response time becomes significantly slower for cold conditions like in the Arctic, where the sensor is not suitable for deriving latent heat fluxes.

Finally the total moisture flux as calculated by the five different moisture signals was compared. In Fig.10 the integrated covariance spectra (ogives, see e.g. Sievers et al., 2015) are shown, normalised by the integral of the cospectrum of w and the Lyman-Alpha humidity. With the closed-path Li2, 98.1% of the Lyman-Alpha value is reached, the small high frequency loss is due to different sensor spacing and tubing. The vibration affected open-path LICOR sensors reach 47% and 83% of the Lyman-Alpha value.

It can be concluded from Fig.9 that the fluxes for frequencies exceeding 1 Hz are negligible for these specific flight conditions. Therefore, the sampling frequency of 20 Hz is sufficient for airborne turbulent humidity fluxes.

The scale of eddies corresponding to the frequency of 1 Hz and the airspeed of $70 \, \mathrm{m \, s^{-1}}$ is around 70 m. Contributions from eddies smaller than the size of few 10 m are negligible. This information is visible in the cospectra and in the ogive functions.

The results emphasise on which scales turbulent transport of humidity takes place: Fluctuations in the frequency range higher than 2 Hz do not contribute significantly to the overall humidity fluxes for these conditions, an air speed of $70 \, \mathrm{m \, s^{-1}}$, altitude of 100 m and the specific surface properties. This is different to flux measurements near ground, where high resolution sampling and close sensor spacing are essential (Caughey and Palmer, 1979; Kaimal and Finnigan, 1994; Bange et al., 2002).

4.4 Spectral analysis of mixing ratio for the Helipod flight

Fig.11 (left) shows the spectra of coherence and phase of the LI7500 signal (time corrected and not time corrected) against the Lyman-Alpha. For a frequency up to 3 Hz, the coherence for the time corrected signal is higher than 0.8, and the phase shift around 0 °, thus the agreement of the two signals is high. The plot on the right represents the humidity flux for both sensors, i.e. the covariance spectra of the humidity and the vertical wind speed component. The areas under the curves are proportional to the humidity fluxes. The Lyman-Alpha and LICOR signals agree perfectly in the frequency range up to 2 Hz. For higher frequencies, the humidity flux is negligible anyway. The effect of the time correction for the humidity fluxes can be seen for frequencies exceeding 0.2 Hz: There are differences in the area under the lines representing the time corrected and uncorrected values. The overall effect is in the range of few percent. As the LI7500 used on the Helipod flew on the Do128 as well (Li3), the excellent agreement with the Lyman-Alpha here demonstrates that the vibrations of the Do128 are the main reason for poor performance there.

5 Recommendations for airborne applications

For calculating turbulent fluxes, the best temporal correlation of the sensors has to be determined first. The time shifts that were determined are not negligible and have to be taken into account. This is a standard procedure in the flux community (Moore, 1986). Time shifts for the LICOR sensors are partly caused by internal processing, partly by different locations of the sensors and tube lengths.

For the Do128 application, three different LICOR sensors were subject to different vibration levels. For the Li1 and Li3 sensors, installed without particular isolation agains vibrations, the correlation with the Lyman-Alpha signal was significantly lower than for the Li2 sensor, which was installed isolated against vibrations. The different covariance spectra of the vibration-affected humidity measurements of the Li1 and Li3 sensors resulted in larger deviations of the latent heat fluxes compared to the latent heat fluxes based on the Lyman-Alpha sensor. The vibration-isolated Li2 sensor showing high correlation with the Lyman-Alpha sensor resulted in comparable latent heat fluxes. However, the spectral behaviour of the vibrations had no direct, linear impact on the humidity spectra of the Li1 and Li3 sensors, but the relationship is more complex. This is currently subject to more detailed investigations.

For the Helipod application with lower vibrations, the humidity fluxes derived from the Lyman-Alpha and the open-path LICOR sensor (Li3) agreed very well after careful sensor calibration to absolute values, and correction of the time lag. Altogether, both open-path and closed-path LICOR sensors are suitable high-resolution hygrometers for airborne applications, if the vibrations are low.

In summary, some precautions have to be taken for employing a LICOR sensor for airborne turbulent humidity flux measurements. Especially the level of vibrations and its impact on the measurements should be evaluated critically, and the spectra of the measurements should be checked for plausibility. Especially for small fluxes, the relative error might be significant. Generally the temporal resolution of the LICOR sensors of 20 Hz is sufficient for humidity flux calculations, as the contribution of frequencies above approximately 2 Hz is negligible, so a 10 times oversampling for a sufficient amplitude retrieval is provided.

Competing interests. The authors declare that they have no conflict of interest.

Author contributions. A.L. wrote the paper, F.P., J.H., A.L. and L.L. performed the data processing and analysis for Helipod and the Do128 flight. P.H. contributed to the analysis. A.L., F.P. and J.H. planned and conducted the Do128 flight with different LICOR humidity sensors. T.S., E.L., K.K. and A.S. planned and conducted the Helipod measurements. All authors commented and contributed to the manuscript.

Acknowledgements. The authors would like to thank Rolf Hankers, Mark Bitter and Helmut Schulz for support with the Do128 intercomparison flight. The authors thank the Alfred Wegener Institute, especially Martin Gehrmann, for providing the LI7200 for the flight, and for fruitful discussions about sensor integration. The authors would like to thank Matthias Cremer from Messwerk GmbH for providing

two accelerometers for the Do128 flight. The authors wish to acknowledge all those who supported the field measurements during the Lena Delta Experiment in 2014. The Helipod flight campaign was supported by the Helmholtz Association of German Research Centres through a Helmholtz Young Investigators Group grant to T.S. (grant VH-NG-821) and is a contribution to the Helmholtz Climate Initiative REKLIM (Regional Climate Change) The authors would like to thank two anonymous referees who helped to improve the manuscript significantly.

References

Aubinet, M., Joly, L., Loustau, D., De Ligne, A., Chopin, H., Cousin, J., Chauvin, N., Decarpenterie, T., and Gross, P.: Dimensioning IRGA gas sampling systems: laboratory and field experiments, Atmos. Meas. Tech., 9, 1361-1367, 2016.

Baer, D.S., Paul, J.B., Gupta, M. and O'Keefe, A.: Sensitivity absorption measurements in a near-infrared region using off-axis integrated-cavity-output spectroscopy, Appl. Phys. B, 75, 261-265, doi:10.1007/s00340-002-0971-z, 2002.

Bange, J., and Roth, R.: Helicopter-borne flux measurements in the nocturnal boundary layer over land - a case study, Boundary-Layer Meteorology, 92, 295-325, 1999.

Bange, J., Beyrich, F., and Engelbart, D.A.M.: Airborne measurements of turbulent fluxes during LITFASS-98: Comparison with ground measurements and remote sensing in a case study, Theor. Appl. Climatol., 73, 35-51, 2002.

Bärfuss, K., Pätzold, F., Altstädter, B., Kathe, E., Nowak, S., Bretschneider, L., Bestmann, U., and Lampert, A.: New Setup of the UAS ALADINA for Measuring Boundary Layer Properties, Atmospheric Particles and Solar Radiation, Atmosphere, Atmosphere, 9, 28; doi:10.3390/atmos9010028, 21 pp., 2018.

Beaton, S.P., and Spowart, M.: UV Absorption Hygrometer for Fast-Response Airborne Water Vapour Measurements, J. Atmos. Ocean. Technolog., 29, 1295-1303, 2012.

Bender, M., Stosius, R., Zus, F., Dick, G., Wickert, J., and Raabe, A.: GNSS water vapour tomography - expected improvements by combining GPS, GLONASS and Galileo observations, Advances in Space Research, 47, 5, 886-897, 2011.

Beringer, J., Hacker, J., Hutley, L.B., Leuning, R., Arndt, S., Amiri, R., Bannehr, L., Cernusak, L.A., Grover, S., Hensley, C., Hocking, D., Isaac, P., Jamali, H., Kanniah, K., Livesley, S., Neininger, B., U, K.T.P., Sea, W., Straten, D., Tapper, N., Weinmann, R., Wood, S., and Zegelin, S.: SPECIAL - Savanna Patterns of Energy and Carbon Integrated across the Landscape, Bull. Am. Met. Soc., doi:10.1175/2011BAMS2948.1+, 1467-1485, 2011.

Buchholz, B., Kühnreich, B., Smit, H.G.J., and Ebert, V.: Validation of an extractive, airborne, compact TDL spectrometer for atmospheric humidity sensing by blind intercomparison, Appl. Phys. B, 110, 249-262, 2013.

Buchholz, B., Böse, N., and Ebert, V.: Absolute validation of a diode laser hygrometer via intercomparison with the German national primary water vapor standard, Appl. Phys. B, 116, 4, 883-899, 2014.

Buchholz, B., Afchine, A., Klein, A., Schiller, C., Krämer, M., and Ebert, V.: HAI, a new airborne, absolute, twin dual-channel, multi-phase TDLAS-hygrometer: background, design, setup, and first flight data, Atmos. Meas. Tech., 9, 1-23, 2016.

Buck, A. L.: Development of an improved Lyman-alpha hygrometer, Atmos. Technol., 2, 213-240, 1973.

Buck, A. L.: The variable-path Lyman-alpha hygrometer and its operating characteristics, B. Am. Meteorol. Soc., 57, 1113-1118, 1976.

Busen, R., and Buck, A.L.: A High-Performance Hygrometer for Aircraft Use: Description, Installation, and Flight Data, J. Atmos. Ocean. Technolog., 12, 73-84, 1995.

Caughey, B.J., and Palmer, S.G.: Some aspects of turbulence structure through the depth of the convective boundary layer, Quart. J. R. Met. Soc., 105, 811-827, 1979.

Chahine, M.T.: The hydrological cycle and its influence on climate, Nature, 359, 373-380, 1992.

Corsmeier, U., Hankers, R., and Wieser, A.: Airborne turbulence measurements in the lower troposphere onboard the research aircraft Dornier 128-6, D-IBUF, Meteorol. Z., 10, 315-329, 2001.

Corsmeier, U., Kalthoff, N., Vogel, B., Hammer, M.-U., Fiedler, F., Kottmeier, C., Volz-Thomas, A., Konrad, S., Glaser, K., Neininger, B., Lehning, M., Jaeschke, W., Memmesheimer, M., Rapenglück, B., and Jakobi, G.: Ozone and PAN Formation Inside and Outside of the Berlin Plume - Process Analysis and Numerical Process Simulation, J. Atmos. Chem., 42, 289-321, 2002.

Crosson, E.R.: A cavity ring-down analyzer for measuring atmospheric levels of methane, carbon dioxide, and water vapor, Appl. Phys. B, 92, 403-408, 2008.

Drüe, C., and Heinemann, G.: Characteristics of intermittent turbulence in the upper stable boundary layer over Greenland, Boundary-Layer Meteorol., 124, 3, 361-381, 2007.

Fahey, D. W., Gao, R.-S., Möhler, O., Saathoff, H., Schiller, C., Ebert, V., Krämer, M., Peter, T., Amarouche, N., Avallone, L. M., Bauer, R., Bozóki, Z., Christensen, L. E., Davis, S. M., Durry, G., Dyroff, C., Herman, R. L., Hunsmann, S., Khaykin, S. M., Mackrodt, P., Meyer, J., Smith, J. B., Spelten, N., Troy, R. F., Vömel, H., Wagner, S., and Wienhold, F. G.: The AquaVIT-1 intercomparison of atmospheric water vapor measurement techniques, Atmos. Meas. Tech., 7, 3177-3213, doi:10.5194/amt-7-3177-2014, 2014.

Foken, T., and Falke, H.: Technical Note: Calibration device for the krypton hygrometer KH20, Atmos. Meas. Tech., 5, 1861-1867, 2012.

Hankers, R.: The Equipment of a Research Aircraft with Emphasis on Meteorological Experiments, Proceedings of the 20th Annual Symposium Society of Flight Test Engineers, 18-21 September 1989, Reno, Nevada, USA, 1989.

Herman, R.L., Ray, E.A., Rosenlof, K.H., Bedka, K.M., Schwartz, M.J., Read, W.G., Troy, R.F., Chin, K., Christensen, L.E., Fu, D., Stachnik, R.A., Bui, T.P., Dean-Day, J.M.: Enhanced stratospheric water vapor over the summertime continental United States and the role of overshooting convection, Atmos. Chem. Phys., 17, 6113-6124, 2017.

Hiller, R.V., Neininger, B., Brunner, D., Gerbig, C., Bretscher, D., Künzle, T., Buchmann, N., and Eugster, W.: Aircraft based CH4 flux estimates for validation of emissions from an agriculturally dominated area in Switzerland, J. Geophys. Res. Atmos., 119, 4874?4887, doi:10.1002/2013JD020918, 2014.

IPCC, 2013: Climate Change 2013: The Physical Science Basis. Contribution of Working Group I to the Fifth Assessment Report of the Intergovernmental Panel on Climate Change [Stocker, T.F., D. Qin, G.-K. Plattner, M. Tignor, S.K. Allen, J. Boschung, A. Nauels, Y. Xia, V. Bex and P.M. Midgley (eds.)]. Cambridge University Press, Cambridge, United Kingdom and New York, NY, USA, 1535 pp, doi:10.1017/CBO9781107415324, 2013.

Kaimal, J.C., and Finnigan, J.J.: Atmospheric Boundary Layer Flows, Their Structure and Measurement, Oxford University Press, New York, 289 pp., 1994.

Kolmogorov, A.: The Local Structure of Turbulence in Incompressible Viscous Fluid for Very Large Reynolds Numbers, Dokl. Akad. Nauk SSSR, 30, 299–303, reprint: Proc. R. Soc. Lond. A, 1991, 434, 9–13, 1941.

van den Kroonenberg A.C., Martin T., Buschmann M., Bange J., and Vörsmann, P.: Measuring the Wind Vector Using the Autonomous Mini Aerial Vehicle M^2AV, J. Atmos. Ocean. Technolog., 25, 1969-1982, 2008.

Lenschow, D.H., Mann, J., and Kristensen, L: How Long is Long Enough When Measuring Fluxes and Other Turbulence Statistics?, J. Atmos. Ocean. Technolog., 11, 661-673, 1994.

Li-Cor LI-7500A Open Path CO2/H2O Gas Analyser Instruction Manual, Li-Cor Inc., $http://www.kohsieh.com.tw/PDF_Files/LICOR/manual/LI-7500A_Manual.pdf$, 2014.

Martin, S., and Bange, J.: The Influence of Aircraft Speed Variations on Sensible Heat-Flux Measurements by Different Airborne Systems, Bound.-Lay. Meteorol., 150, 153-166, 2014.

May, R.D.: Open-path, near-infrared tunable diode laser spectrometer for atmospheric measurements of H_2O, J., Geophys. Res., 103, D15, 19161-19172, 1998.

Metzger, S., Burba, G., Burns, S.P., Blanken, P.D., Li, J., Luo, H., and Zulueta, R.C.: Optimization of an enclosed gas analyzer samplnig system for measuring eddy covariance fluxes of H_2O and CO_2, Atmos. Meas. Tech., 9, 1341-1359, 2016.

Moore, C.J.: Frequency response corrections for eddy correlation systems, Boundary-Layer Meteorology, 37, 17-35, 1986.

Pillai, D., Gerbig, C., Ahmadov, R., Rödenbeck, C., Kretschmer, R., Koch, T., Thompson, R., Neininger, B., and Lavrié, J. V.: High-resolution simulations of atmospheric CO2 over complex terrain - representing the Ochsenkopf mountain tall tower, Atmos. Chem. Phys., 11, 7445-7464, 2011.

Ramanathan, V., Cess, R.D., Harrison, E.F., Minnis, P., Barkstrom, B.R., Ahmad, E., and Hartmann, D.: Cloud-radiative forcing and climate: Results from the earth radiation budget experiment, Science, 243, 57?63, 1989.

Schmitgen, S., Geiß, H., Ciais, P., Neininger, B., Brunet, Y., Reichstein, M., Kley, D., and Volz-Thomas, A.: Carbon dioxide uptake of a forested region in southwest France derived from airborne CO2 and CO measurements in a quasi-Lagrangian experiment, J. Geophys. Res., 109, D14302, doi:10.1029/2003JD004335, 2004.

Schneider, M., Romero, P.M., Hase, F., Blumenstock, T., Cuevas, E., and Ramos, R.: Continuous quality assessment of atmospheric water vapour measurement techniques: FTIR, Cimel, MFRSR, GPS, and Vaisala RS92, Atmos. Meas. Tech., 3, 323–338, 2010.

Siebert, H., Beals, M., Bethke, J., Bierwirth, E., Conrath, T., Dieckmann, K., Ditas, F., Ehrlich, A., Farrell, D., Hartmann, S., Izaguirre, M.A., Katzwinkel, J., Nuijens, L., Roberts, G., Schäfer, M., Shaw, R.A., Schmeissner, T., Serikov, I., Stevens, B., Stratmann, F., Wehner, B., Wendisch, M., Werner, F., and Wex, H.: The fine-scale structure of the trade wind cumuli over Barbados - an introduction to the CARRIBA project, Atmos. Chem. Phys., 13, 10061-10077, 2013.

Sievers, J., Papakyriakou, T., Larsen, S.E., Jammet, M.M., Rysgaard, S., Sejr, M.K., and Sorensen, L.L.: Estimating surface fluxes using eddy covariance ans numerical ogive optimization, Atmos. Chem. Phys., 15, 2081–2103, 2015.

Sodemann, H., Aemisegger, F., Pfahl, S., Bitter, M., Corsmeier, U., Feuerle, F., Graf, P., Hankers, R., Hsiao, G., Schulz, H., Wieser, A., and Wernli, H.: The stable isotopic composition of water vapour above Corsica during the HyMeX SOP1 campaign: insight into vertical mixing processes from lower-tropospheric survey flights, Atmos. Chem. Phys., 17, 6125–6151, 2017.

Trenberth, K. E., Jones, P. D., Ambenje, P., Bojariu, R., Easterling, D., Klein Tank, A., Parker, D., Rahimzadeh, F., Renwick, J. A., Rusticucci, M., Soden, B., and Zhai, P.: Observations: Surface and Atmospheric Climate Change, in: Climate Change 2007: The Physical Science Basis. Contribution of Working Group I to the Fourth Assessment Report of the Intergovernmental Panel on Climate Change, edited by: Solomon, S., Qin, D., Manning, M., Chen, Z., Marquis, M., Averyt, K. B., Tignor, M., and Miller, H. L., Cambridge University Press, Cambridge, United Kingdom and New York, NY, USA, 2007.

Twohy, C.H., Schanot, A.J., and Cooper, W.A.: Measurement of Condensed Water Content in Liquid and Ice Clouds Using an Airborne Counterflow Virtual Impactor, J. Atmos. Ocean. Technolog., 14, 197-202, 1997.

Wildmann, N., Kaufmann, F., and Bange, J.: An inverse-modelling approach for frequency response correction of capacitive humidity sensors in ABL research with small remotely piloted aircraft (RPA), Atmos. Meas. Tech., 7, 3059– 3069, 2014.

Zhou, Y.P., Xu, K.-M., Sud, Y.C., and Betts, A.K.: Recent trends of the tropical hydrological cycle inferred from Global Precipitation Climatology Project and International Satellite Cloud Climatology Project data, J. Geophys. Res., 116, D09101, doi:10.1029/2010JD015197, 16 pp., 2011.

Zondlo, M.A., Paige, M.E., Massick, S.M., and Silver, J.A., Vertical cavity laser hygrometer for the National Science Foundation Gulfstream-V aircraft, J. Geophys. Res., 115, D20309, doi:10.1029/2010JD014445, 14 pp., 2010.

Figure 1. The three LICOR sensors integrated into the Do128 during a humidity intercomparison flight: a) LI7500A on the nose boom (Li1), b) LI7200 in the cabin with an inlet near the LICOR sensor on the roof (Li2), c) LI7500 on the roof (Li3), and d) the Do128 equipped with additional sensors during the flight (last photo courtesy of Uwe Bethke).
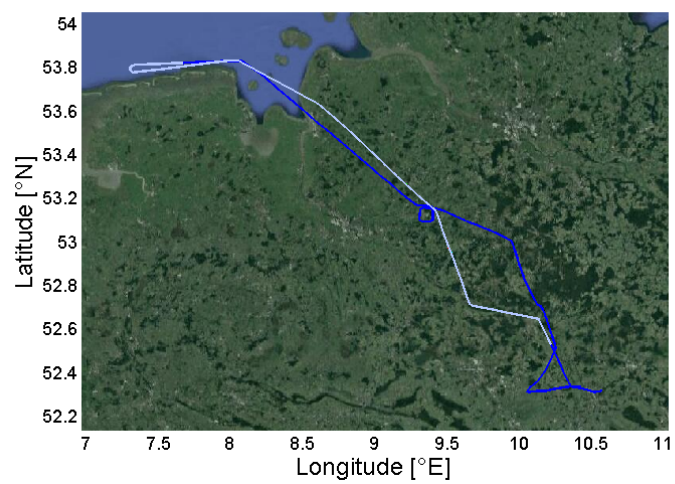
Figure 2. Flight track of the Do128 aircraft above the North German Plain during the humidity intercomparison flight. The part of the data used for the analysis is displayed in white colour. The picture was taken from Google Maps, accessed on 29 May 2017.
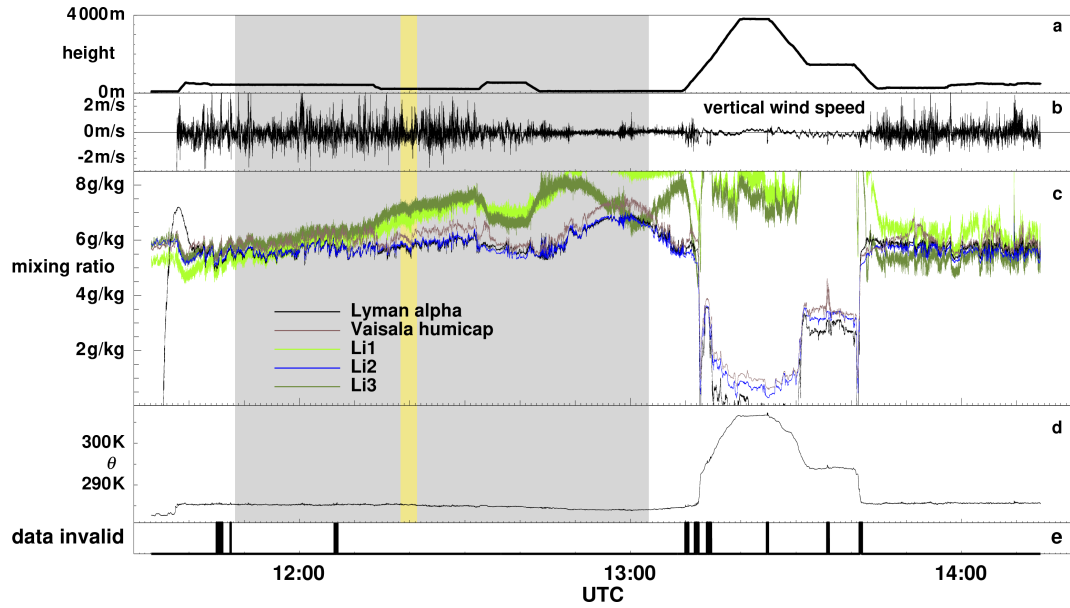
Figure 3. Overview of the flight with the Do128 on 23 October 2015. Subplot (a) shows the height, (b) the vertical wind speed, indicating the strength of atmospheric turbulence. Subplot (c) shows the time series of the mixing ratio measured by Lyman-Alpha (black), Vaisala Humicap (purple), closed-path Li2 (blue), open-path Li1 at the nose boom (bright green), and closed-path Li3 on the cabin roof (olive). Subplot (d) provides the potential temperature. Subplot (e) shows the periods of invalid data, e.g. when radio communication disturbed the signals. For the spectral analysis, the part of the data shaded in grey was used, excluding segments with invalid data, e.g. disturbance by radio communication. The vibration data is analysed for the flight segment indicated in yellow.
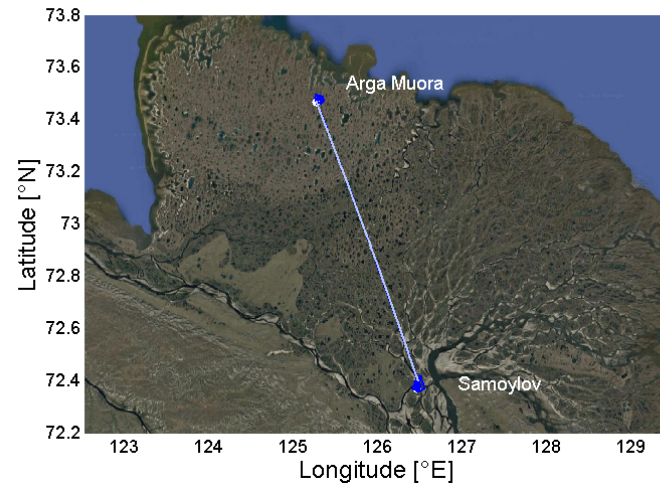
Figure 4. Flight track of the Helipod in the Lena River Delta for the measurement flight on 14 August 2014. The flight started at Samoylov Station and went towards Arga-Muora in the North-West. The part of the data used for the analysis is displayed in white colour. The picture was taken from Google Maps, accessed on 29 May 2017.
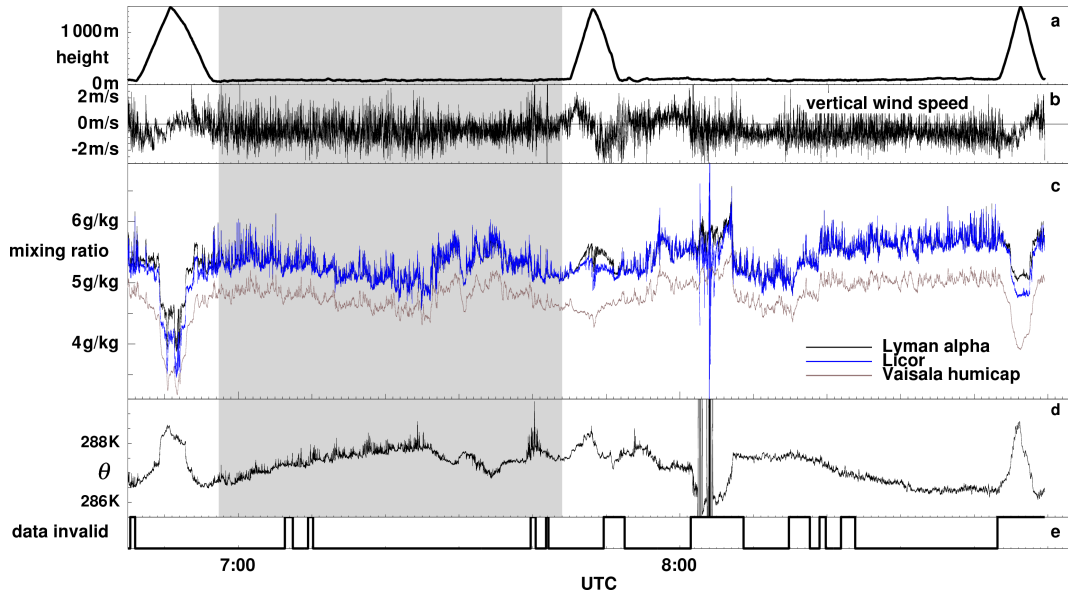
Figure 5. Overview of the flight with the Helipod on 14 August 2014. Subplot (a) shows the height, (b) the vertical wind speed, indicating the strength of atmospheric turbulence. Subplot (c) shows the time series of the mixing ratio measured by Lyman-Alpha (black), Vaisala Humicap (purple) and the open-path Li3 (blue). Subplot (d) represents the potential temperature. Subplot (e) shows the parts of the flight with data that was excluded from the analysis for various reasons (e.g. impact of rain). For the spectral analysis, the part of the data shaded in grey was used, excluding segments indicated in the lowermost panel.
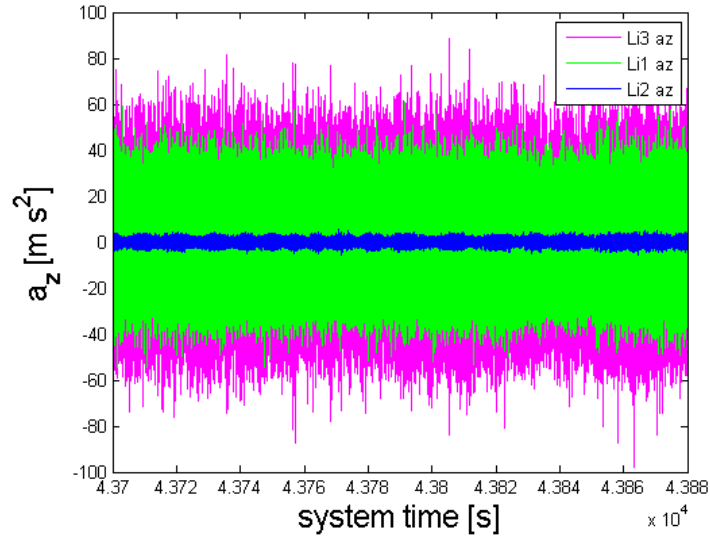
Figure 6. Time series of the accelerations in z direction of the three LICOR sensors during a flight section of 3 min duration on 23 October 2013, illustrating the vibrations the LICOR sensors were exposed to. The flight section took place above agricultural land at 220 m altitude. The acceleration measurements of this flight section are representative for other flight sections at different, but constant altitude. The acceleration measurements at the Li1 are shown in green, at the Li2 in blue, and at the Li3 in magenta. The data were obtained during the part of the flight indicated in yellow in Fig. 3.
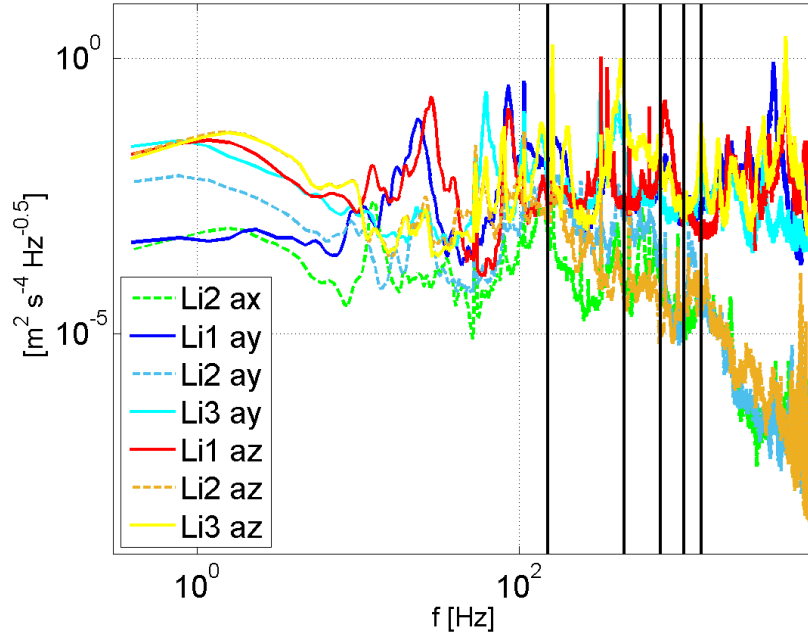
Figure 7. Acceleration spectra measured at the three humidity sensors Li1, Li2 and Li3 during the Do128 flight on 23 October 2015 for the same flight section as in Fig.6. The colours blue and red indicate the accelerations of Li1 (y and z direction, respectively), the colours cyan and yellow indicate the accelerations of Li3 (y and z direction, respectively), and the dashed lines in green, bright blue and ocher indicate the accelerations of Li2 (x, y and z direction). The vertical black bars indicate the critical frequencies of 150 Hz and odd harmonics 450 Hz, 750 Hz, 1050 Hz, 1350 Hz according to the manufacturer. The data were obtained during the part of the flight indicated in yellow in Fig. 3.
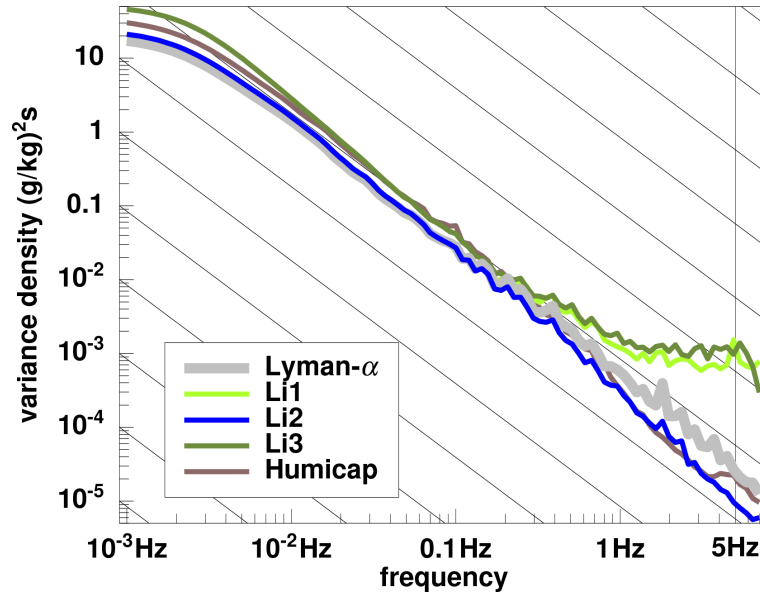
Figure 8. Powerspectra (variance density) of the different humidity sensors on the Do128, Li1 in bright green, Li2 in blue, Li3 in olive, Lyman-Alpha in grey, Humicap in purple. The spectra are averaged over the data of the time series shaded in grey in Fig.3. The lines have the slope of -5/3 according to Kolmogorov theory.
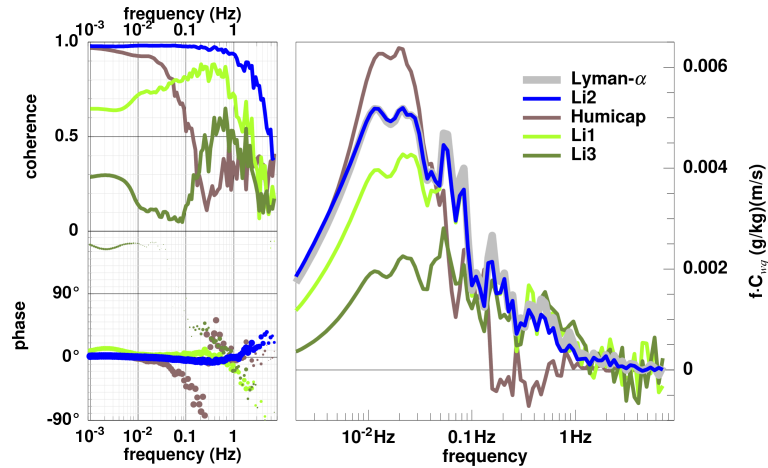
Figure 9. Left: Phase and coherence of the different LICOR humidity sensors on the Do128 related to the Lyman-Alpha sensor, with the same colour code as in Fig.8. In the diagram of phase shift, higher coherence is represented by larger dot size. Right: Co-spectra of humidity from the different sensors and vertical wind speed on the Do128, multiplied by the frequency. The area under the curves is proportional to the humidity fluxes. The data are averaged over the data of the time series shaded in grey in Fig.3.
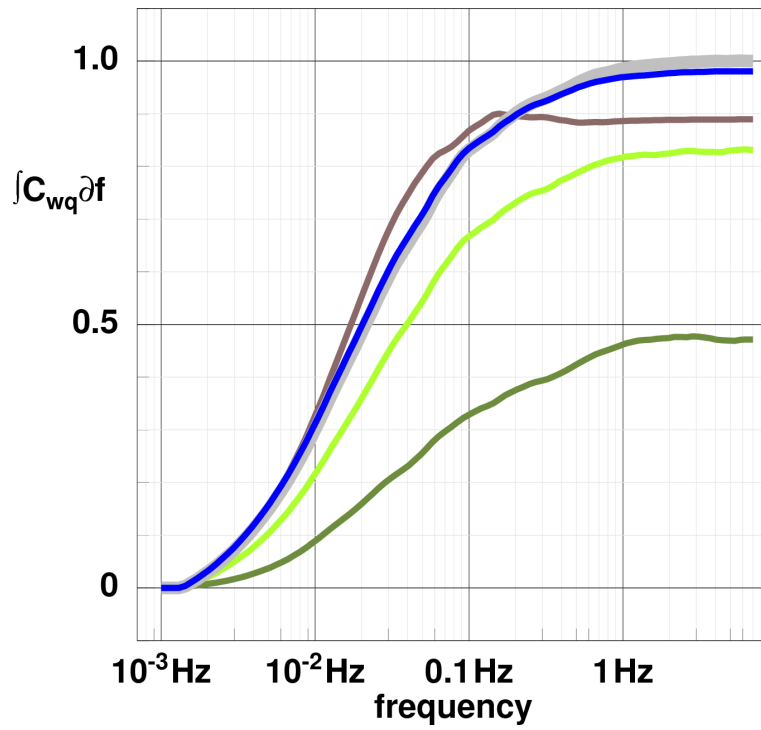
Figure 10. Ogive functions (integral over the latent heat fluxes) for the Do128 flight on 23 October 2015. The colours indicate the same humidity sensors as in Fig.8.
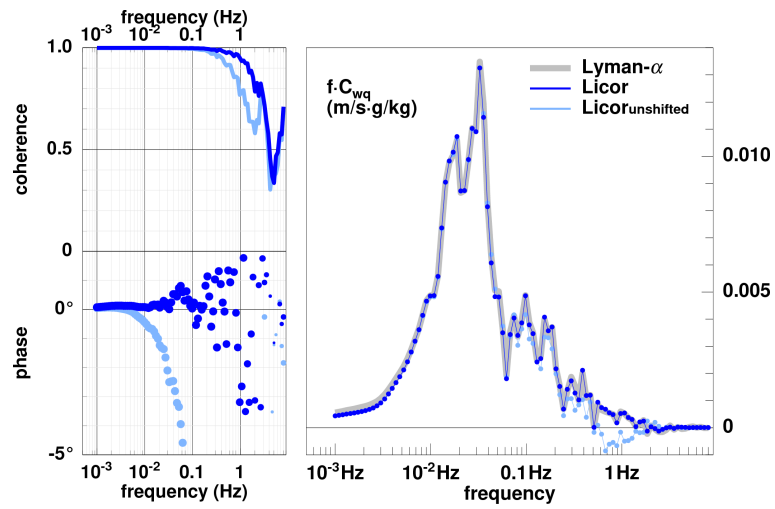
Figure 11. Phase shift and coherence spectra of the shifted (darker blue) and unshifted (light blue) signal of the LICOR sensor on the Helipod (left) and co-spectra of humidity from the different sensors and vertical wind speed multiplied by the frequency (right) on the Helipod flight. The area under the curves is proportional to the humidity fluxes. The flight part indicated in the time series in Fig.5 in grey was used.